Band gap temperature-dependence of close-space sublimation grown Sb$_2$Se$_3$ by photo-reflectance

Max Birkett, [iD] Wojciech M. Linhart, Jessica Stoner, et al.

COLLECTIONS

Paper published as part of the special topic on Earth Abundant Materials in Solar Cells

View Online   Export Citation   CrossMark

ARTICLES YOU MAY BE INTERESTED IN

Optical properties of amorphous and polycrystalline Sb$_2$Se$_3$ thin films prepared by thermal evaporation
Applied Physics Letters **107**, 043905 (2015); https://doi.org/10.1063/1.4927741

Selenization of Sb$_2$Se$_3$ absorber layer: An efficient step to improve device performance of CdS/Sb$_2$Se$_3$ solar cells
Applied Physics Letters **105**, 083905 (2014); https://doi.org/10.1063/1.4894170

Scalable and efficient Sb$_2$S$_3$ thin-film solar cells fabricated by close space sublimation
APL Materials **7**, 041105 (2019); https://doi.org/10.1063/1.5090773

Band gap temperature-dependence of close-space sublimation grown Sb₂Se₃ by photo-reflectance

Max Birkett,[1,a,b] Wojciech M. Linhart,[2,a] Jessica Stoner,[1] Laurie J. Phillips,[1] Ken Durose,[1] Jonathan Alaria,[1] Jonathan D. Major,[1] Robert Kudrawiec,[2] and Tim D. Veal[1,b]

[1]*Stephenson Institute for Renewable Energy, Department of Physics, University of Liverpool, Liverpool L69 7ZF, United Kingdom*
[2]*Institute of Experimental Physics, Wroclaw University of Technology, 50-370 Wroclaw, Poland*

The candidate photovoltaic absorber antimony selenide Sb₂Se₃ has been prepared by the commercially attractive close-space sublimation method. Structure, composition, and morphology are studied by x-ray diffraction, scanning electron microscopy, and energy dispersive spectroscopy. Large rhubarb-like grains favorable for photovoltaics naturally develop. The temperature-dependence of the direct band gap is determined by photoreflectance between 20 and 320 K and is well described by the Varshni and Bose–Einstein relations, blue-shifting with decreasing temperature from 1.18 to 1.32 eV. The 300 K band gap matches that seen in high quality single-crystal material, while the 0 K gap is consistent with that found in first-principles calculations, further supporting the array of beneficial photovoltaic properties indicated for this material. © *2018 Author(s). All article content, except where otherwise noted, is licensed under a Creative Commons Attribution (CC BY) license (http://creativecommons.org/licenses/by/4.0/).* https://doi.org/10.1063/1.5027157

Research in thin-film photovoltaics seeks high-performance, earth-abundant, low-toxicity, and low-cost alternatives to established light-absorbing media such as cadmium telluride (CdTe) or copper indium gallium selenide (CIGS).[1] Significant complications exist in all current research directions: copper zinc tin sulfo-selenide (CZTSSe) cells have achieved efficiencies of 12.6%,[2] yet performance may ultimately be constrained by non-radiative recombination losses at defects and grain boundaries;[3] organic metal-halide perovskites (e.g., $CH_3NH_3PbI_3$ with 22% efficiency)[2] may be limited by poor stability and Pb-toxicity concerns;[3] while attractive inorganic binaries such as SnS and FeS_2 presently show disappointing efficiencies, with only CdTe surpassing 10%.[4]

Recently, the inorganic semiconductor antimony selenide (Sb₂Se₃) has attracted interest as a potential ideal photovoltaic (PV) absorber.[3] Such claims are supported by encouragingly rapid growth in Sb₂Se₃ solar cell efficiencies,[5] which have recently achieved 6.5%[6] despite minimal interest since the earliest work.[7] Particular beneficial factors include a desirable 1.2 eV band gap for photovoltaics;[8–10] very strong absorption exceeding 10^5 cm^{-1} before 2 eV (1000 times that of silicon);[7,11,12] a 1D crystal structure leading to intrinsically benign grain boundaries[3] (minimizing non-radiative recombination losses); high stability and low-toxicity;[5,8,12] reduced fabrication costs due to a binary elemental composition, single phase, and low-temperature deposition (low melting point of 885 K);[12] and earth-abundance, giving a 2016 raw material cost of 5 US cent/m^2 micron-thick film.[8,12] Away from thin-film PV, Sb₂Se₃ has been studied for applications in thermoelectrics,[13] thermophotovoltaics,[14] switching,[15] optical storage,[16] optoelectronics,[17] and 2D anisotropic materials.[18]

Sb₂Se₃ (antimonselite) is a binary chalcogenide with the stibnite crystal structure (orthorhombic space group *Pnma*; equivalent to *Pbnm*),[4,19–21] comprising 1D ribbons of an Sb_4Se_6 repeat-unit with

---

[a]M. Birkett and W. M. Linhart contributed equally to this work.
[b]Authors to whom correspondence should be addressed: max.birkett@gmail.com and T.Veal@liverpool.ac.uk

distinct Sb(1) and Sb(2) sites (coordinated, respectively, with 6 and 7 Se) with four Sb_2Se_3 per unit cell. The 1D ribbons extend only in the *Pnma* $\langle 010 \rangle$ direction, bound by covalent Sb–Se bonds; weak van der Waals forces bind the ribbons in the $\langle 100 \rangle$ and $\langle 001 \rangle$ directions.[3] First principles work finds that the ribbon edges have few mid-gap states, beneficial to minimize non-radiative recombination and suggesting that 1D materials may offer an attractive design principle for photovoltaics.[3] Reduced conductivity is seen perpendicular to the ribbon axes as carriers must hop between ribbons:[3] so crystal orientation is particularly important for cell design.[5] Optimization of band-alignment and stability through window- and hole-transport layer selection are key research areas (as elsewhere).[22,23] While the precursory CdS/Sb_2Se_3 layout (inherited from CdTe) allows the detrimental diffusion of Cd atoms across the junction interface,[5] performance improves with TiO_2/Sb_2Se_3 or ZnO/Sb_2Se_3 architectures[5,24] and with a supplementary PbS hole-transport layer.[6] Prior Sb_2Se_3 synthesis routes have included thermal evaporation,[3,5,8,18,25,26] chemical bath deposition,[12,26] Bridgman method,[9] solution or spin-coating,[12] RF sputtering,[26] and spray-deposition or pyrolysis.[25,26] This paper reports large Sb_2Se_3 crystal grains grown by close-space sublimation (CSS), perhaps the simplest physical vapor deposition method. CSS is highly attractive to commercial PV vendors and is often favored for CdTe cell fabrication (including champion cells). Specific advantages include low-costs, high deposition rates (e.g., several microns of CdTe within minutes), configuration versatility, and ease of scaling-up to meet production targets.[27]

Despite the interest in Sb_2Se_3, considerable variance is seen in reports on the nature and magnitude of the band gap, which is variously claimed to be either indirect, ranging from 1.0 to 1.5 eV (either allowed[8,10,11,25,26] or forbidden[9]), or direct[8,11] ranging from 1.2 to 1.9 eV. The fundamental gap is generally considered to be indirect with a direct gap lying at ~0.1 eV to higher energy,[8] leading to very strong optical absorption: highly desirable in a PV absorber; in contrast, silicon has rather weak absorption until the direct onset at 3.2 eV. Part of the deviation in the reported gaps lies in the suitability of fitting expressions raised to some exponent, such as $(\alpha \hbar \omega) = A \left(\hbar \omega - E_g \right)^m$,[28,29] to experimental absorption spectra (which are non-trivially determined even after careful assessment of transmission and reflection spectra). In the case of Sb_2Se_3, where experimental and first-principles studies suggest closely spaced direct and indirect gaps and perhaps multiple overlapping transitions,[30] the suitability of attempting fits with a single such expression is particularly questionable in the absence of further assumptions. Variable material quality is another key factor complicating band gap assessment. Amorphous material is often reported[7–9,11,18,25,26] in low-temperature Sb_2Se_3 deposition and always has a higher gap than crystalline material. An amorphous-to-crystalline transition[7,8,11,16,26,31] occurs upon annealing above 200 °C, yet while crystalline material is easily detected by x-ray diffraction, amorphous phase fractions are more difficult to quantify. In non-stoichiometric material, the band gap is reported to increase quadratically with increasing Se content[26] or in the presence of an oxygen impurity[5,7] (perhaps differing from the $Fd\bar{3}m$ Sb_2O_3 phase) which is removed after annealing in N_2 and Se vapor at 300 °C. Allowing also for potential polycrystalline disorder, each of these factors likely necessitates the consideration of an Urbach tail in any fit to the absorption onset.[26]

Band gap temperature evolution (arising from thermal lattice expansion and the electron-phonon interaction)[32,33] may have significant photovoltaic implications: with efficiencies falling by as much as 0.1% K^{-1} as reverse saturation current and band gap reduction each increase with temperature.[34,35] In prior temperature-dependent work,[9] the single-crystal band gap increased by 80 meV as the temperature lowered from 293 to 80 K (possibly also supported by the evolution of the direct gap in a recent polycrystalline study).[8] To investigate the Sb_2Se_3 band gap unambiguously in commercially important CSS-grown, polycrystalline material without the aforementioned difficulties, the temperature-evolution of the direct gap is studied here using photo-reflectance (PR) spectroscopy between 20 and 320 K; as a derivative method, PR is perhaps a more powerful means of assessing interband critical points than has been applied previously.[28] Simultaneously, material quality is carefully examined to identify key factors relevant to this important deposition route.

The close-space sublimation (CSS) reactor consists of an evacuated chamber containing an Sb_2Se_3 powder tray (99.99% purity, Alfa Aesar) set ~5 mm below a float-glass substrate. Powder temperature is set by an infrared heater, which indirectly heats the substrate due to its proximity. Deposition is initiated by abruptly ramping to 450 °C under 10 Torr N_2 and halted after 17 min by

raising to 200 Torr N_2 with no heating. Six polycrystalline films were deposited, four of which were annealed (at 150, 300, 350, and 400 °C) for 20 min in N_2 at 1 bar.

The Sb_2Se_3 *Pnma* phase was verified with a Rigaku SmartLab x-ray diffractometer (XRD), with a monochromated 9 kW Cu-$K\alpha_1$ rotating anode and HyPix-3000 detector, using a θ:2θ scan between 10° and 60° 2θ at 1° min^{-1}. Scanning electron microscopy (SEM) with a JEOL JSM-6610 at 20 keV revealed films of rhubarb-like crystallites of typical diameter 1 μm and length 4 μm, with 84% substrate coverage, see Fig. 1. Cross-sectional SEM found a 2.6 μm film thickness. Energy dispersive spectroscopy (EDS) at 20 keV with an Oxford Instruments INCA x-act silicon drift detector averaged over 0.6 mm^2 for 60 s. Photoreflectance spectra were taken between 20 and 320 K with the sample mounted in a Janis CSS-100 closed-cycle helium refrigerator managed by a programmable temperature controller and illuminated by a 150 W tungsten-halogen probe-beam and a 405 nm semiconductor pump laser (modulated by a mechanical chopper at 290 Hz). The probe and pump beams were focused to a diameter of ~3 mm at the sample, with the reflected light dispersed by a Horiba ᴛʀɪᴀx-550 monochromator (1200 lines mm^{-1} and 55 cm focal-length) and detected via a thermoelectrically cooled InGaAs pin photodiode. Phase sensitive detection of the PR signal was achieved with a lock-in amplifier. No photoluminescence was seen from these samples.

Photoreflectance on all films at 300 K found similar ~1.18 eV direct band gaps (see Fig. 1 of the supplementary material). The film annealed at 300 °C had highest coverage and was selected for further temperature-dependent studies. As the Sb_2Se_3 optical properties are crystallinity- and orientation-dependent, XRD was performed to confirm the *Pnma* phase and to assess the mosaic texture (due to rhubarb-shaped crystallites) and any impurity phases. Figure 1 shows Rietveld refinement of the Sb_2Se_3 *Pnma* structure, giving lattice parameters a = 11.7758(5) Å, b = 3.9763(2) Å, and c = 11.6288(6) Å, comparable with those of Voutsas[19] to 0.2%. While the many reflections seen suggest good crystal quality, texture optimization should improve PV performance. As often seen in Sb_2Se_3 films, significant preferential orientation is found; the best-fit has a (212)-texture with intensities modeled as $\exp(-G\alpha_{hkl}^2)$, where G = 1.44 and α_{hkl} is the acute angle between the (*hkl*) and (212) plane normals (Fig. 2 of the supplementary material shows a poor fit without a texture model). This texture has the crystallite ribbon axes preferentially inclined from the substrate while suppressing crystallites with ribbon axes either parallel or normal to the substrate. Such (212)- or (112)-textures have been associated with champion photovoltaic cell efficiencies,[3,5] thought due to optimal conductivity into the junction region. Some confusion over the ribbon axis direction arises from the different *Pnma* and *Pbnm* settings of space group 62 used, respectively, by Voutsas[19] and Tideswell,[20] which align the ribbon axes along either the *b*- or *c*-axes (short axes). Rotating the *Pbnm* coordinate system (*a*, *b*, *c*) (and plane Miller indices) gives the preferred *Pnma* lattice parameters (*b*, *c*, *a*).[36] Some residuals remain in Fig. 1, yet attempts to more accurately determine the ribbon orientation, both experimentally (via broad rocking scans) and indirectly by studying reflection intensities (see Fig. 3 of the supplementary material), failed to support other texture models. No refinement of atomic positions, stoichiometry, or phase fractions was attempted due to the texture. A weak secondary Sb_2O_3 phase (α-Sb_2O_3; space group $Fd\bar{3}m$; senarmontite)[37] was inferred, the (222) reflection at 27.6° 2θ Cu $K\alpha$ being by far the strongest in the Sb_2O_3 pattern.[38] Six of these planes cut the unit cell, so the signal may arise from a few nanometers of surface Sb_2O_3 developing on exposure to air post-growth.

The prevalence of columnar crystallites indicates a Volmer–Weber (island) growth mode on this float glass substrate, although other growth modes are not excluded. Interestingly, cross-sectional SEM finds many columns inclined at ~46° from the substrate [see Fig. 1(a)] corresponding to the (212)-texture seen in XRD. The morphology from atop shows many similarly inclined crystallites [see Fig. 1(c)]; the smooth, pillar-like nature of these suggests that growth occurs in the ribbon-axis direction. EDS revealed primary Sb, Se, O, and C lines, with weak secondaries associated with the float-glass substrate (Si, Ca, Na, Mg, Ti). The primary glass line (Si) is strongly suppressed in Sb_2Se_3 regions, indicating a negligible glass contribution. The quantitative atomic fractions are consistent with a stoichiometric Sb_2Se_3 phase to the limits of measurement.

The temperature-evolution of the Sb_2Se_3 PR spectra is depicted in Fig. 2(a). One strong feature associated with an interband optical transition redshifts and broadens with increasing temperature *T*.
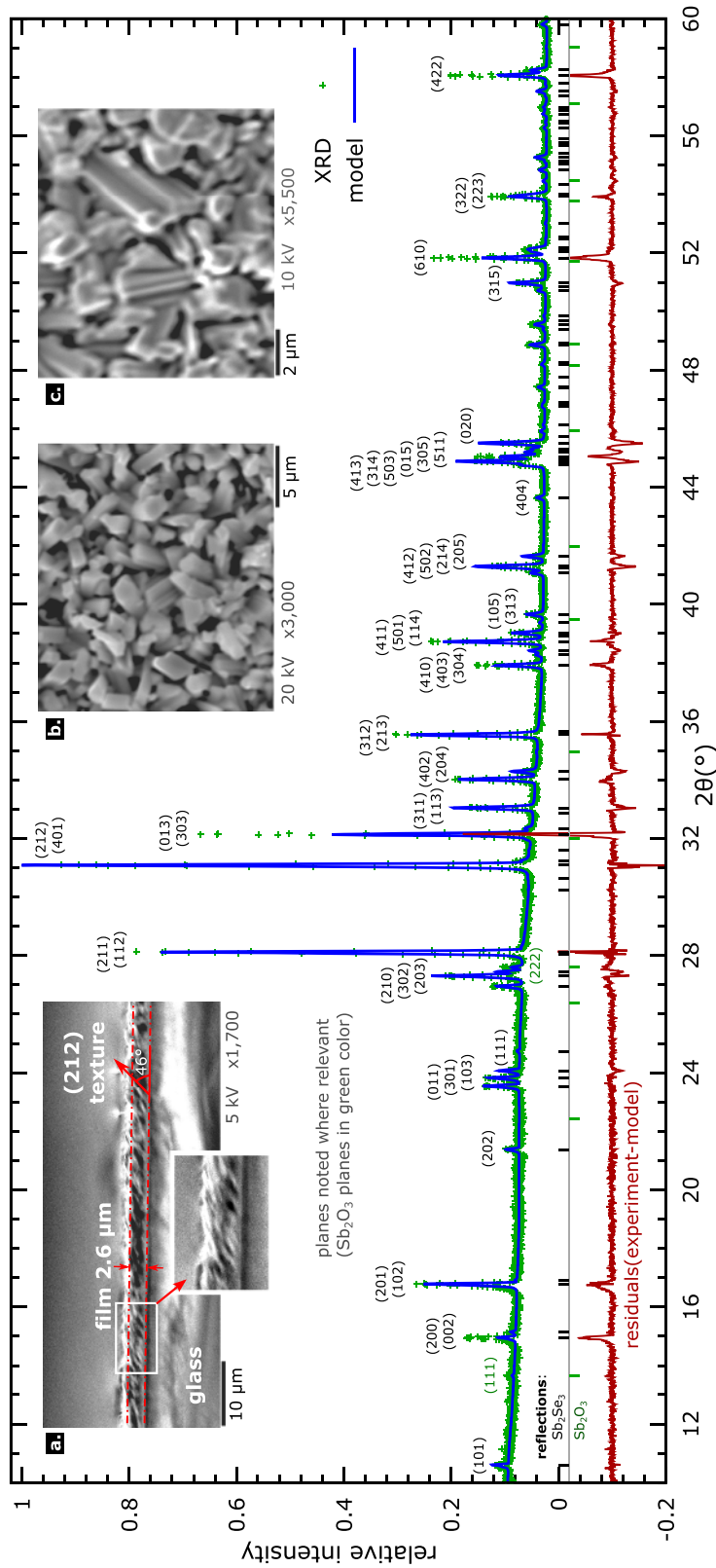
FIG. 1. X-ray diffraction (Cu $K\alpha$) and Rietveld refinement of the Sb_2Se_3 *Pnma* structure, giving lattice parameters comparable with Voutsas[19] to 0.2%. A (212)-texture associated with champion PV performance is seen. A weak secondary α-Sb_2O_3 phase ($Fd\bar{3}m$) is just evident at 27.6° 2θ. Cross-sectional SEM image (a) shows a 2.6 μm thick film with a pillar-like texture; many pillars are inclined at ~46° from the substrate, corresponding to the (212) texture seen in XRD. SEM images (b) and (c) show the film morphology from atop, with large pillar-like crystallites indicating a Volmer–Weber growth mode, with growth perhaps occurring in the ribbon-axis direction.
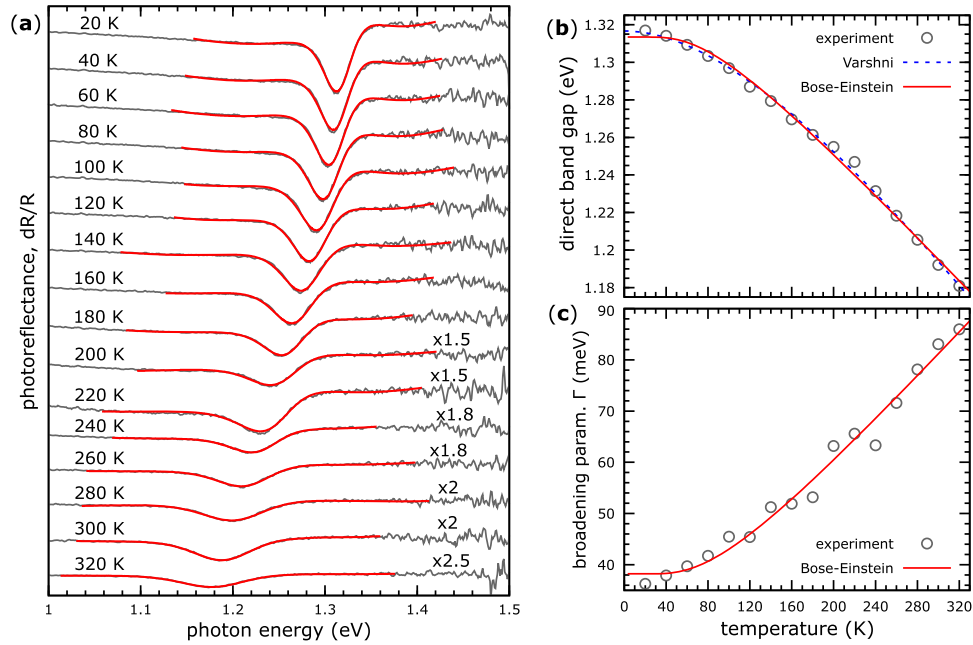
FIG. 2. (a) Temperature-dependent Sb_2Se_3 photoreflectance spectra (gray lines) in the vicinity of an interband optical transition, fitted by the Aspnes model of Eq. (1) (red lines). (b) Temperature-evolution of the interband transition energy $E_0(T)$ given by Eq. (1), together with the Varshni (solid line) and Bose–Einstein (dashes) fits of Eqs. (2) and (3). (c) Evolution of the broadening parameter $\Gamma_0(T)$, fitted (solid line) by the Bose–Einstein model of Eq. (4).

An Aspnes[39] model in the optical transition energy $E_0(T)$ is fitted to these spectra,

$$\frac{\delta R(\hbar\omega)}{R(\hbar\omega)} = \mathrm{Re}\left[Ce^{i\theta}\left\{\hbar\omega - E_0(T) + i\Gamma(T)\right\}^{-m}\right], \tag{1}$$

where $\hbar\omega$ is the photon energy, $R(\hbar\omega)$ is the intrinsic probe-beam reflectivity, $\delta R(\hbar\omega)$ is the reflectivity difference under the pump beam, $\Gamma(T)$ is a broadening parameter, and C and θ denote the respective line amplitude and phase. The exponent m sets the optical transition type: with excitonic character ($m = 2$) seen at low temperatures and interband character ($m = 2.5$) dominating at higher temperatures; however, PR resonances are often significantly broadened by material inhomogeneities, complicating the assessment of excitonic and interband contributions. Therefore, the PR spectra of Fig. 2(a) are each fitted by a single interband resonance ($m = 2.5$) attributed to the fundamental transition between the valence-band maximum and conduction-band minimum.

The band gap temperature dependence $E_0(T)$ is shown in Fig. 2(b). The gap increases from 1.180 to 1.316 eV ($\Delta E_0 = 136$ meV) as the temperature decreases from 320 to 20 K. This temperature dependence is fitted with the empirical Varshni[40] expression,

$$E_0(T) = E_0(0) - \frac{\alpha T^2}{\beta + T}, \tag{2}$$

where $E_0(0)$ is the zero Kelvin band gap. The Varshni parameters $E_0(0)$, α, and β determined for Sb_2Se_3 are, respectively, 1.317 eV, 0.90 meV K^{-1}, and 358 K; the α parameter differs slightly from that (0.93 meV K^{-1}) obtained previously by optical absorption measurements over a smaller temperature range.[41] The band gap $E_0(T)$ is also fitted with a Bose–Einstein model, which accounts for the coupling of bands with a temperature-dependent phonon population,[42,43]

$$E_0(T) = E_0(0) - \frac{2\alpha_B}{\exp\left(\frac{\Theta_B}{T}\right) - 1}, \tag{3}$$

where α_B is an average electron-phonon interaction strength and Θ_B is an average phonon temperature. The fitted $E_0(0)$, α_B, and Θ_B parameters are, respectively, 1.313 eV and 70.9 meV and 236 K. Notably, the α_B parameter fitted here is almost half that (125 meV) reported previously.[41]

The temperature-dependence of the Aspnes broadening parameter $\Gamma(T)$ from Eq. (1) is shown in Fig. 2(c). Material inhomogeneities lead to a broadening of ~38 meV at low temperature, which then increases with temperature due to increasing phonon interactions, as described by the Bose–Einstein formula,

$$\Gamma_0(T) = \Gamma_0(0) + \frac{\Gamma_{LO}}{\exp\left(\frac{\Theta_{LO}}{T}\right) - 1},\tag{4}$$

where Γ_{LO} is an electron-longitudinal optical (LO) phonon coupling constant and Θ_{LO} is the LO phonon temperature. Fitting (4) to the Aspnes broadening parameter $\Gamma(T)$ determined experimentally from (1) and Fig. 2(a) gives the curve in Fig. 2(c) and respective parameters Γ_{LO} and Θ_{LO} of 58.2 meV and 257 K. The LO phonon temperature and Varshni β parameter of (2) have similar magnitudes, possibly as these are associated through the phonon population and Debye temperature (262.78 K, 292.50 K, or 240 K, respectively, from Refs. 21 and 44).

While the 1.18 eV optical gaps determined here by PR at 300 K are broadly consistent with prior work,[4,15] particularly two temperature-dependent single-crystal and polycrystalline transmission studies,[8,9] the various practical complexities of crystallinity, orientation, stoichiometry, and morphology, combined with assorted experimental issues (e.g., transmission spectra omitting reflection assessment; different band gap types, and fitting approaches), combine to produce a literature which gives a confusing picture of the Sb_2Se_3 band gap. Some of this confusion is perhaps part due to unreliable reflection and transmission spectra caused by the topography-induced variable film thickness (low albedo halted ellipsometry work on these samples). Our approach then is to favor least vulnerable characterization methods, such as modulation spectroscopy, whilst endeavoring to assess such complications where possible. As a differential method PR is unaffected by scattering losses so may study textured samples in cases where reflection/transmission spectroscopy would fail due to diffuse scattering; PR probes critical points in the joint density of states so is ideal for studying direct transitions whilst being insensitive to indirect transitions[45] and avoiding complications from energy- and orientation-dependent absorption magnitudes. Having said this, a consensus does emerge on the raised ~1.35 eV optical gap seen in amorphous material;[7,8,10,25,26,46] the 1.18 eV PR band gap and numerous XRD reflections suggest negligible amorphous content in this CSS material.

The band gap rises by 110 meV between 300 and 80 K; this is reasonable, given an 80 meV change in single crystals.[9] No significant differences are evident between the Varshni and Bose–Einstein fits. Zero Kelvin band gaps are noteworthy because density-functional theory (DFT) calculations determine material properties at 0 K. To this end, the 1.317 eV Varshni 0 K direct gap is supported impressively by a recent HSE06 1.324 eV direct gap,[47] as well as previous *GW* studies.[30,48] Such calculations find an indirect gap very slightly below the direct transition (e.g., $\Delta E_g = 25$ meV).[47] This configuration is experimentally supported by the absence of photoluminescence (as previously),[8] i.e., photoexcited carriers recombine non-radiatively. Whilst the Varshni fit of Ref. 8 gives a similar 0 K gap, this work has certain other issues which illustrate some of the above complexities: it is not justifiable to impose that spectra above and below 150 K, respectively, arise exclusively from either indirect- or direct-gap transitions, given that absorption from both types is expected at all temperatures; the indirect onset omits a phonon energy $\hbar\omega$ (giving perhaps a $2\hbar\omega \sim 50$ meV error) and in any case should be orders of magnitude weaker than the direct term, so fits are only sensible in the region immediately below the direct gap. Otherwise, the PR-determined Varshni parameters are very reasonable. For comparison, the E_0, α, and β parameters reported[49] for the sister material Sb_2S_3 are 2.1 eV, 0.7 meV K^{-1}, and 350 K, while the Sb_2Se_3 α and β parameters are well within the typical range for Varshni parameters: as seen by respective mean (and standard deviation) α and β values of 0.6(5) meV K^{-1} and 400(500) K for fits to 37 common semiconductors.[40,50]

While the rhubarb-like morphology seen in Fig. 1 suggests voids and detrimental short-circuit or shunt conductive paths ruinous of photovoltaic efficiencies, solar cell deposition occurs atop metal oxide or CdS window layers. Our device work[47] depositing identically grown material onto TiO_2 and CdS shows continuous Sb_2Se_3 layers at the interface and achieves attractive efficiencies of 5.5%, so

such morphology is not necessarily a barrier to performance goals. Mitigation of such pinholes in other absorbers employs treatments filling voids with neutral material, e.g., with the polymer P3HT in CdTe.[51] Identification of an ideal window-layer (e.g., ZnO, SnO_2: F, TiO_2, or CdS) and combined optimization alongside the Sb_2Se_3 deposition should lead to Sb_2Se_3-based devices with competitive efficiencies, e.g., see the evolution with different ZnO textures in Fig. 1(d) of Ref. 5.

In conclusion, commercially relevant polycrystalline CSS-grown Sb_2Se_3 material has been studied by temperature-dependent PR spectroscopy. A strong PR signal fitted via an Aspnes model finds a band gap which increases monotonically from 1.180 to 1.316 eV ($\Delta E_0 = 136$ meV) as the temperature decreases from 320 to 20 K. The 300 K band gap is consistent with single-crystal material, and the temperature-dependence is well described by the Varshni and Bose–Einstein models.

See supplementary material for the experimental and fitted photoreflection (PR) spectra for all six CSS samples at 300 K, for Rietveld refinement of the Sb_2Se_3 structure without preferential orientation (via the XRD pattern of the sample annealed at 300 °C), and for a texture analysis of the 300 °C-annealed film which presents relevant texture coefficients and reveals that the crystallites preferentially arrange so that Sb_2Se_3 ribbons are inclined from the substrate.

[1] J. D. Major, R. E. Treharne, L. J. Phillips, and K. Durose, Nature **511**, 334 (2014).

[2] M. A. Green, K. Emery, Y. Hishikawa, W. Warta, E. D. Dunlop, D. H. Levi, and A. W. Y. Ho-Baillie, Prog. Photovolt: Res. Appl. **25**, 3 (2017).

[3] Y. Zhou, L. Wang, S. Chen, S. Qin, X. Liu, J. Chen, D.-J. Xue, M. Luo, Y. Cao, Y. Cheng, E. H. Sargent, and J. Tang, Nat. Photonics **9**, 409 (2015).

[4] K. Zeng, D.-J. Xue, and J. Tang, Semicond. Sci. Technol. **31**, 063001 (2016).

[5] L. Wang, D.-B. Li, K. Li, C. Chen, H.-X. Deng, L. Gao, Y. Zhao, F. Jiang, L. Li, F. Huang, Y. He, H. Song, G. Niu, and J. Tang, Nat. Energy **2**, 17046 (2017).

[6] C. Chen, L. Wang, L. Gao, D. Nam, D. Li, K. Li, Y. Zhao, C. Ge, H. Cheong, H. Liu, H. Song, and J. Tang, ACS Energy Lett. **2**, 2125 (2017).

[7] S. Messina, M. Nair, and P. Nair, J. Electrochem. Soc. **156**, H327 (2009).

[8] C. Chen, W. Li, Y. Zhou, C. Chen, M. Luo, X. Liu, K. Zeng, B. Yang, C. Zhang, J. Han, and J. Tang, Appl. Phys. Lett. **107**, 043905 (2015).

[9] F. Kosek, J. Tulka, and L. Štourač, Czech. J. Phys. B **28**, 325 (1978).

[10] R. Mueller and C. Wood, J. Non-Cryst. Solids **7**, 301 (1972).

[11] H. El-Shair, A. Ibrahim, E. A. El-Wahabb, M. Afify, and F. A. El-Salam, Vacuum **42**, 911 (1991).

[12] Y. Zhou, M. Leng, Z. Xia, J. Zhong, H. Song, X. Liu, B. Yang, J. Zhang, J. Chen, K. Zhou, J. Han, Y. Cheng, and J. Tang, Adv. Energy Mater. **4**, 1301846 (2014).

[13] T.-Y. Ko, M. Shellaiah, and K. W. Sun, Sci. Rep. **6**, 35086 (2016).

[14] P. M. Fourspring, D. M. DePoy, T. D. Rahmlow, Jr., J. E. Lazo-Wasem, and E. J. Gratrix, Appl. Opt. **45**, 1356 (2006).

[15] N. S. Platakis and H. C. Gatos, Phys. Status Solidi A **13**, K1 (1972).

[16] P. Arun, A. G. Vedeshwar, and N. C. Mehra, J. Phys. D **32**, 183 (1999).

[17] E. Montrimas and A. Pažera, Thin Solid Films **34**, 65 (1976).

[18] H. Song, T. Li, J. Zhang, Y. Zhou, J. Luo, C. Chen, B. Yang, C. Ge, Y. Wu, and J. Tang, Adv. Mater. **29**, 1700441 (2017).

[19] G. P. Voutsas, A. G. Papazoglou, P. J. Rentzeperis, and D. Siapkas, Z. Kristallogr. - Cryst. Mater. **171**, 261 (1985).

[20] N. W. Tideswell, F. H. Kruse, and J. D. McCullough, Acta Cryst. **10**, 99 (1957).

[21] H. Koc, A. M. Mamedov, E. Deligoz, and H. Ozisik, Solid State Sci. **14**, 1211 (2012).

[22] A. W. Welch, L. L. Baranowski, P. Zawadzki, C. DeHart, S. Johnston, S. Lany, C. A. Wolden, and A. Zakutayev, Prog. Photovoltaics: Res. Appl. **24**, 929 (2016).

[23] T. J. Whittles, T. D. Veal, C. N. Savory, A. W. Welch, F. W. D. S. Lucas, J. T. Gibbon, M. Birkett, R. J. Potter, D. O. Scanlon, A. Zakutayev, and V. R. Dhanak, ACS Appl. Mater. Interfaces **9**, 41916 (2017).

[24] C. Chen, Y. Zhao, S. Lu, K. Li, Y. Li, B. Yang, W. Chen, L. Wang, D. Li, H. Deng, F. Yi, and J. Tang, Adv. Energy Mater. **7**, 1700866 (2017).

[25] E. Černošková, R. Todorov, Z. Černošek, J. Holubová, and L. Beneš, J. Therm. Anal. Calorim. **118**, 105 (2014).

[26] E. El-Sayad, J. Non-Cryst. Solids **354**, 3806 (2008).

[27] N. Amin and K. S. Rahman, in *Modern Technologies for Creating the Thin-Film Systems and Coatings*, 1st ed. (InTech, Rijeka, 2017), Chap. 18, pp. 361–363.

[28] P. Y. Yu and M. Cardona, *Fundamentals of Semiconductors*, 4th ed. (Springer, 2010).

[29] C. Hamaguchi, *Basic Semiconductor Physics*, 2nd ed. (Springer, 2010).

[30] R. Vadapoo, S. Krishnan, H. Yilmaz, and C. Marin, Phys. Status Solidi B **248**, 1521 (2011).

[31] K. Y. Rajpure, C. D. Lokhande, and C. H. Bhosale, Thin Solid Films **311**, 114 (1997).

[32] M. Cardona, Solid State Commun. **133**, 3 (2005).

[33] C. Yu, Z. Chen, J. J. Wang, W. Pfenninger, N. Vockic, J. T. Kenney, and K. Shum, J. Appl. Phys. **110**, 063526 (2011).

[34] P. Singh and N. Ravindra, Sol. Energy Mater. Sol. Cells **101**, 36 (2012).

[35] P. Löper, D. Pysch, A. Richter, M. Hermle, S. Janz, M. Zacharias, and S. Glunz, Energy Procedia **27**, 135 (2012).

[36] E. F. Bertaut, in *International Tables for Crystallography, Volume A: Space-Group Symmetry*, Space Group 62 in Table 4.3.2.1, 1st ed. (International Union of Crystallography, 2006), Chap. 4.3, p. 66.

[37] D. Orosel, R. E. Dinnebier, V. A. Blatov, and M. Jansen, Acta Crystallogr., Sect. B: Struct. Sci. **68**, 1 (2012).

[38] C. Svensson, Acta Crystallogr., Sect. B: Struct. Sci. **31**, 2016 (1975).

[39] D. Aspnes, Surf. Sci. **37**, 418 (1973).

[40] Y. Varshni, Physica **34**, 149 (1967).

[41] F. I. Mustafa, S. Gupta, N. Goyal, and S. K. Tripathi, J. Optoelectron. Adv. Mater. **11**, 2019 (2009).

[42] S. Logothetidis, L. Via, and M. Cardona, Phys. Rev. B **31**, 947 (1985).

[43] P. Lautenschlager, M. Garriga, S. Logothetidis, and M. Cardona, Phys. Rev. B **35**, 9174 (1987).

[44] *Landolt-Börnstein–Group III Condensed Matter Volume 41C: Non-Tetrahedrally Bonded Elements and Binary Compounds I*, edited by O. Madelung, U. Rössler, and M. Schulz (Springer-Verlag Berlin Heidelberg, 1998).

[45] J. Kopaczek, M. P. Polak, P. Scharoch, K. Wu, B. Chen, S. Tongay, and R. Kudrawiec, J. Appl. Phys. **119**, 235705 (2016).

[46] C. Wood, Z. Hurych, and J. Shaffer, J. Non-Cryst. Solids **8**, 209 (1972).

[47] L. J. Phillips, C. N. Savory, P. J. Yates, H. Shiel, O. S. Hutter, S. Mariotti, L. Bowen, K. Durose, D. O. Scanlon, and J. D. Major, "A scalable synthesis approach to antimony selenide solar cells," Nat. Commun. (submitted).

[48] M. R. Filip, C. E. Patrick, and F. Giustino, Phys. Rev. B **87**, 205125 (2013).

[49] A. Vedeshwar, J. Phys. III **5**, 1161 (1995).

[50] S. Adachi, *Properties of Group-IV, III-V and II-VI Semiconductors*, 1st ed. (Wiley, 2005).

[51] J. Major, L. Phillips, M. A. Turkestani, L. Bowen, T. Whittles, V. Dhanak, and K. Durose, Sol. Energy Mater. Sol. Cells **172**, 1 (2017).